Effect of Strong Seismic Action on Piled Raft with DMW Grid in Soft Ground via 3-D Finite Element Analysis

3次元有限要素解析による軟弱地盤中の格子状改良壁併用パイルド・ラフト基礎の大地震時挙動に関する検討

Kiyoshi Yamashita 山下 清*1 Yoshimasa Shigeno 重野 喜政*2 Junji Hamada 濱田 純次*3

Summary

Performance of a piled raft foundation combined with the deep mixing wall (DMW) grid in soft ground under strong earthquakes are investigated by the authors via a three-dimensional nonlinear dynamic finite element analysis. In this paper, seismic response analysis of the piled raft system supporting a building with a natural period near that of the ground (LS model) was conducted to load substantial inertial force from the superstructure on the piled raft system. Based on the analysis results including the base-isolated building (BI model) previously published, it was found that the bending moments of the piles in LS model are decreased significantly by the presence of the DMWs as in the same way in BI model. It was also found that although the inertial forces from the superstructure in LS model are large, the bending moments of piles in the piled raft are more affected by the kinematic ground movement than the inertial force from the structure, and in BI model the sectional forces of the piles are generated mostly by the kinematic effect.

Keywords: piled raft foundation, deep mixing wall grid, soft ground, strong earthquake, pile stress, 3-dimensional FEM, dynamic analysis

梗　概

軟弱地盤における格子状地盤改良体を併用したパイルド・ラフト基礎の大地震時の挙動を，地盤の非線形性を考慮した3次元動的FEM解析により検討している。本報では基礎に大きな慣性力を作用させるため，上部構造の固有周期が地盤の固有周期に近い建物（LSモデル）について地震応答解析を行った。LSモデルと既発表の免震建物（BIモデル）の結果にもとづき，建物慣性力および地盤変位が杭の断面力に及ぼす影響について考察した。その結果，LSモデルにおいてもBIモデルと同様に，改良体がある場合は杭の曲げモーメントが大幅に減少することがわかった。またパイルド・ラフト基礎では，杭の曲げモーメントに及ぼす慣性力の影響は上部構造の慣性力が大きいLSモデルにおいても地盤変位の影響より小さいこと，BIモデルでは杭の断面力はほぼ地盤変位の影響により生じることがわかった。

キーワード：パイルド・ラフト基礎，格子状地盤改良，大地震，杭断面力，3次元FEM，動的解析

1 INTRODUCTION

In recent years, piled raft foundation, which mean a piled foundation combining piles and raft response in a design, has been used in many countries. The most effective application of piled rafts occurs when the raft can provide adequate load capacity but the settlement and/or differential settlements of the raft alone exceed the allowable values, hence favorable situations may be soil profiles consisting of relatively stiff clays and relatively dense sands (Poulos, 2017). On the other hand, unfavorable situations are profiles with very soft clayey soils and/or requifiable soils near the surface of the raft. To cope with this, an advanced piled raft system called "piled raft combined with cement deep mixing wall (DMW) grid" has been developed (Yamashita et al.,

*1 Executive Manager, Research & Development Institute, Dr. Eng. 技術研究所 専門役 博士(工学)
*2 Group Leader, Research & Development Institute 技術研究所 先端技術部 数理科学グループ長
*3 General Manager, Geotechnical & Foundation Engineering Department, Research & Development Institute, Dr. Eng. 技術研究所 地盤・基礎部長 博士(工学)

2011). The DMW grid is used as a countermeasure of soil liquefaction under the raft as well as to increase the bearing capacity of the raft foundation. Moreover, the DMW grid is expected to mitigate stresses induced in the piles under strong earthquakes. Poulos (2016) has pointed out that seismic action will induce additional lateral forces in the structure and also induce lateral motions in the ground supporting the structure, and that the additional forces and motions can be induced in the foundation system via two mechanisms, i.e., inertial forces developed by the lateral excitation of the structure and kinematic forces induced by the action of ground movements. Hence, the effects of the inertial and kinematic forces should be considered in the seismic design of the piled raft system. Yamashita et al. (2012) reported the seismic observation records of a piled raft combined with the DMW grid in soft ground supporting a 12-story base-isolated building at the time of the 2011 off the Pacific coast of Tohoku Earthquake. Hamada et al. (2019) investigated seismic behavior of piled raft with soil-cement wall supporting a slender building in soft clayey soil using a geotechnical centrifuge. Yamashita et al. (2018) conducted the dynamic analysis of the piled raft system supporting the 12-story base-isolated building under strong earthqakes using a three-dimensional finite element model.

In this paper, to investigate the inertial effect on the piled raft system, seismic response analysis of the 12-story building with a natural period near that of the ground in which substantial inertial force is loaded on the piled raft system was conducted. Based on the analysis results including the previous study on the base-isolated building, the inertial and kinematic effects on the piled raft system under strong earthquakes are discussed, concerning the influence of the presence of the DMWs on the sectional forces of the piles.

2 SOIL CONDITIONS AND FOUNDATION DESIGN

Figure 1(a) illustrates a schematic view of a 12-story residensial building and its foundation with a typical soil profile. The building is located in Tokyo and a reinforced-concrete structure with a seismic base-isolation system (Yamashita et al., 2012). The total load in the structural design was 198.8 MN (average pressure over the raft was 200 kPa). The subsoil consists of very soft to medium clayey soil layers to a depth of 43 m, underlain by dense sandy layers. The groundwater table appears about 1.8 m below the ground surface, and it was ascertained that the silty sand near the ground surface had potential for liquefaction with a peak ground acceleration of 0.2 g. Hence, to prevent liquefaction of the silty sand as well as to provide adequate load capacity of the raft, a piled raft combined with DMW grid (which were extended to a depth of 16 m with the bottom being embedded in the stiffer silty clay) was employed. Sixteen piles consisted of SC (steel pipe-concrete composite) pile in the top portion and PHC pile in the bottom portion. The toes of the piles reached the very dense sand-and-gravel layer, which were used to reduce the settlement to acceptable levels. Figure 1(b) illustrates the foundation plan with the layout of the piles and the DMW grid where the area replacement ratio (area of DMWs divided by total area) is 0.25.

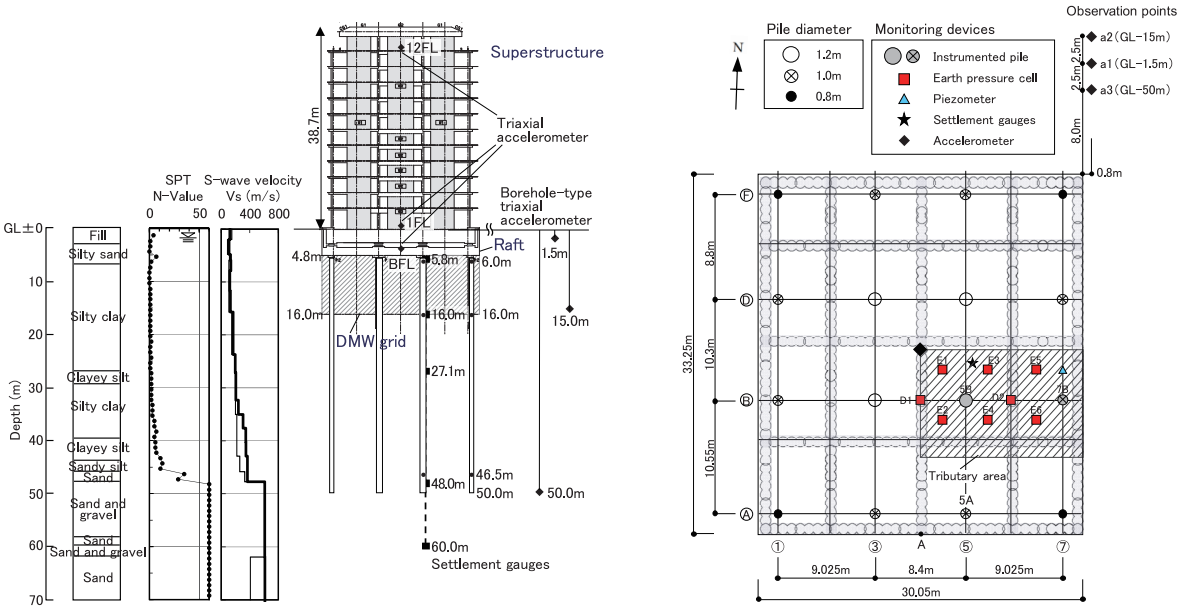

(a) Cross section with soil profile (b) Foundation plan with locations of monitoring devices

Fig. 1 Schematic of building and foundation with soil profile

3 DYNAMIC FINITE ELEMENT ANALYSIS

Figure 2 illustrates the 3-dimentional FE model of the 12-story building with the foundation and the ground, which was used in the previous numerical study (Yamashita et al., 2018). The lateral boundaries are periodic boundaries while the bottom boundary is a viscous one. The concrete walls and floors of the superstructure were modeled using elastic shell elements, while the steel columns were modeled with elastic beam elements. The raft was modeled with elastic solid elements. The damping ratios of the steel and the concrete were set to 2%. The piles were modeled using beam elements, while the voids were modeled with rigid bar elements in order to consider the shape and the volume of the piles. The material properties of the piles are listed in Table 1.

In the previous study, the 12-story building with a base isolation system (in which the natural period of the superstructure was fully larger than that of the ground) was used. In this paper, to load substantial inertial force from the superstructure on the piled raft system, the building in which the natural period of the superstructure (T_b) is near that of the ground (T_g) is modeled. In order to make T_b close to T_g=0.86 s, linear springs were added to the base of the superstructure whose fixed based natural period is 0.59 s. Figure 3 illustrates the schematic of the lateral load vs. displacement relations for the linear spring and tri-linear spring. The natural period of the superstructure with the linear spring is 0.87 s (which is close to T_g). The tri-linear spring presented by Hamada et al. (2014) was used for the superstructure with the base isolation system in the previous study. The natural period of the base-isolation system is 4.6 s in the design where the bi-linear spring shown in Fig. 3 is used and the base isolation devices fully function against the Level 2 motions. Herein, the superstructure with the linear spring (T_b=0.87 s) and the superstructure with the base isolation system (T_b=4.6 s) are denoted as LS model and BI model, respectively.

As the three-dimensional constitutive model of soil, the Yoshida model for multi-dimensional analysis was used (Tsujino et al., 1994). The stress-strain relationship is based on a nonlinear elastic model, then the yielding function is only used as a strength criterion of the Mohr-Coulomb model. Figure 4 shows the G/G_0-γ and h-γ characteristics of the soil obtained from cyclic triaxial tests of the undisturbed samples. Figure 5 shows the shear wave velocity (V_s) profile derived from a P-S logging, together with the V_s profile used in the analysis. To evaluate the induced stresses in the DMWs against their capacity, the

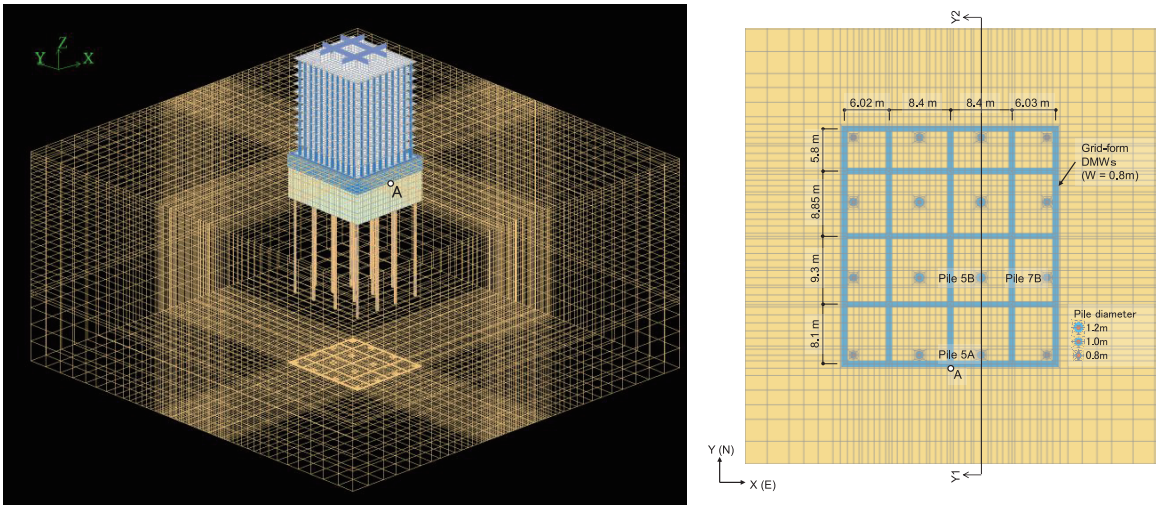

(a) Three-dimensional finite element model (b) Top view of piles and DMW grid

Fig. 2 Finite element model of soil-foundation-structure

Table 1 Dimensions and material properties of piles

Pile diameter (mm)	Young's modulus (MPa)	Density ρ (t/m^3)	Damping ratio (%)	A_e of SC pile (m^2)	I_e of SC pile (m^4)	A_e of PHC pile (m^2)	I_e of PHC pile (m^4)
800	40000	2.5	2.0	0.3268	0.02199	0.2441	0.01455
1000	40000	2.5	2.0	0.4649	0.04899	0.3633	0.03437
1200	40000	2.5	2.0	0.6714	0.10316	0.5054	0.06958

A_e : Equivalent cross-sectional area
I_e : Equivalent area moment of inertia

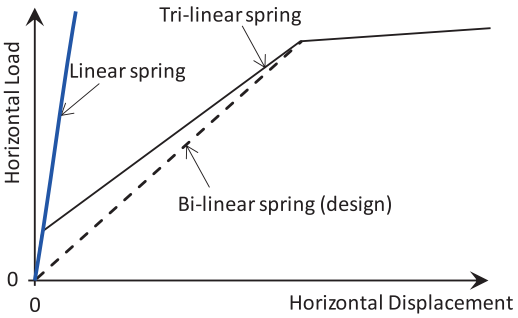

Fig. 3 Schematic of load vs. displacement relations of linear and tri-linear springs

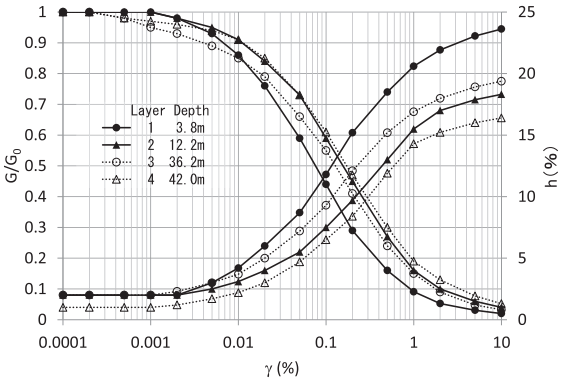

Fig. 4 Strain-dependent characteristics of unimproved soil

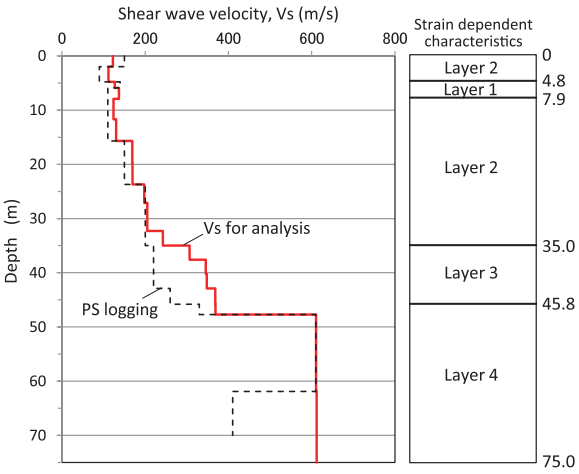

Fig. 5 Profile of optimized initial shear wave velocity and strain dependence characteristics in analysis

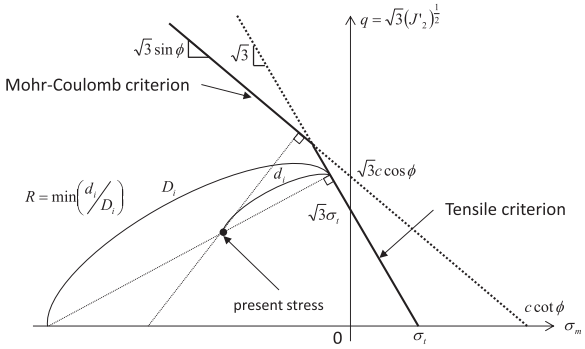

Table 2 Properties of stabilized soil and parameters used in Hayashi-Hibino model

Density ρ (t/m^3)	F_c (MPa)	Tensile strength $\sigma_t = 0.2F_c$ (MPa)	Cohesion c=0.3F_c (MPa)	Friction angle φ (degree)	Initial shear modulus G_0 (MPa)	Poisson's ratio ν_0	Damping ratio h (%)	Nonlinear parameter a	G/G_0 after failure
2.0	2.6	0.52	0.78	30	500	0.26	5.0	1.0	1.0e-5

Hayashi-Hibino model was used as a two criteria model (Motojima et al., 1978). The criteria of the Hayashi-Hibino model are shown in Fig. 6. The model is a nonlinear elastic model which is able to evaluate tensile and shear failure of stabilized soil. The properties of the stabilized soil and the parameter used in Hayashi-Hibino model are listed in Table 2.

As strong earthquake motions, input motion of Level 2 earthquake with mean return period of approximately 500 years was employed (Building Standard Law of Japan, 2000). Figure 7 shows the code-defined acceleration response spectrum of the Level 2 motion on the engineering bedrock. Figure 8 shows the acceleration time history of the input motion using Kobe and Hachinohe phase data on the bedrock (2E). The input motion was applied horizontally in the NS direction at a depth of 75 m.

Table 3 Numerical cases

Case	Input motion phase	DMWs
LS model	Kobe	Yes
	Kobe	No
	Hachinohe	Yes
	Hachinohe	No
BI model	Kobe	Yes
	Kobe	No
	Hachinohe	Yes
	Hachinohe	No
Null mass model	Kobe	Yes
	Kobe	No
	Hachinohe	Yes
	Hachinohe	No

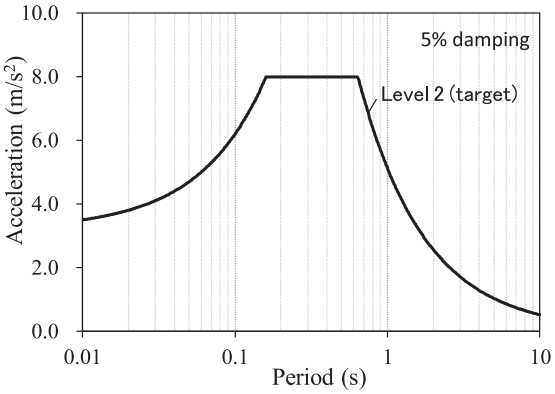

Fig. 7 Acceleration response spectrum of Level 2 motions on engineering bedrock

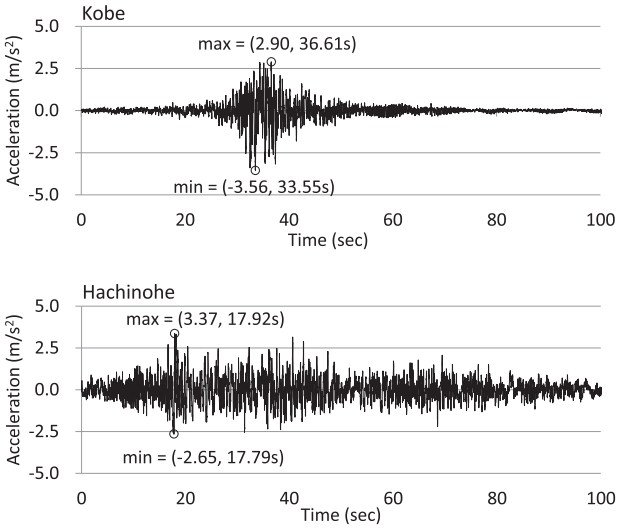

Fig. 8 Input acceleration waveforms at 75 m depth (2E)

Numerical cases of the LS and BI models are listed in Table 3. Furthermore, the analyses using null mass model were conducted (mentioned in 5.3). The software is an in-house program called MuDIAN (Shiomi et al., 1993). It is parallelized using the hybrid parallel method, and is able to analyze a large-DOF model at high speed (Shigeno et al., 2014). The analysis results of the BI model as well as details in the finite element model, modeling and properties of the soil etc. are presented in the previous numerical study.

4 ANALYSIS RESULTS

Figure 9 shows the acceleration response spectra (5% damping) of the top of the structure at the center, the raft bottom at point A (shown in Fig. 2) and the free-field ground surface under Kobe and Hachinohe phases, together with the spectrum of the bedrock at 75 m depth (E+F). The response at the free field ground was obtained from the one-dimensional analysis using a soil column model, and an initial natural period of the ground (T_g=0.86 s) was derived from Fourier spectrum ratio of the linear elastic ground response. In comparison of the response spectra of the top of the structure in LS model with that of the free-field surface, marked amplification at a period of about 1.0 s (which is slightly larger than T_b=0.87 s) is seen under both phase motions. In contrast, in BI model, significant de-amplification over periods less than 2 s is seen, and obvious amplification at the top of the structure around a period of 4.0 s (which is near the natural period in the design) is seen. In comparison of the response spectra of the free-field surface and the raft with that of the bedrock, substantial amplification over periods of 1-1.5 s is seen under both phase motions. Considering T_g=0.86 s, this may be attributed to the strain-dependent nonlinearity in the soil deposit. The nonlinearity results in a lengthening of T_g and leads to T_g>T_b under Level 2 motions. In LS model over the periods of 1-1.5 s, the amplification of the raft with DMWs is lower than that of the ground while the amplification of the raft without DMWs is higher than that of the ground. In BI model, the amplification of the raft is considerably lower than that of the ground regardless of the presence of the DMWs. In the following, the analysis results under the Kobe phase are presented and discussed.

Figure 10 shows the peak acceleration profiles of the superstructure at center, the DMWs and soil under point A and the free field ground under the Kobe phase. The maximum accelerations at the top of the superstructure are 9.2-9.5 m/s^2 and 1.6-1.8 m/s^2 in the LS and BI models, respectively, while that at the ground surface is 3.3 m/s^2. Namely, the maximum accelerations at the top in LS model are amplified to nearly three times of the maximum acceleration at the ground surface, while those in BI model are reduced to around 50% of the maximum acceleration at the ground surface. Figure 11 shows the peak horizontal displacement profiles of the superstructure at center, the DMWs and soil under point A and the free field ground. The displacements are relative values to those at 49.9 m depth. The increase in displacement to the top of the superstructure is obvious in the LS model, while the increase is quite small in BI model. The peak ground displacement at the surface is 0.22 m. It is seen that in both LS and BI models, the peak displacements of the raft with the DMWs just under the raft are markedly smaller than those without DMWs.

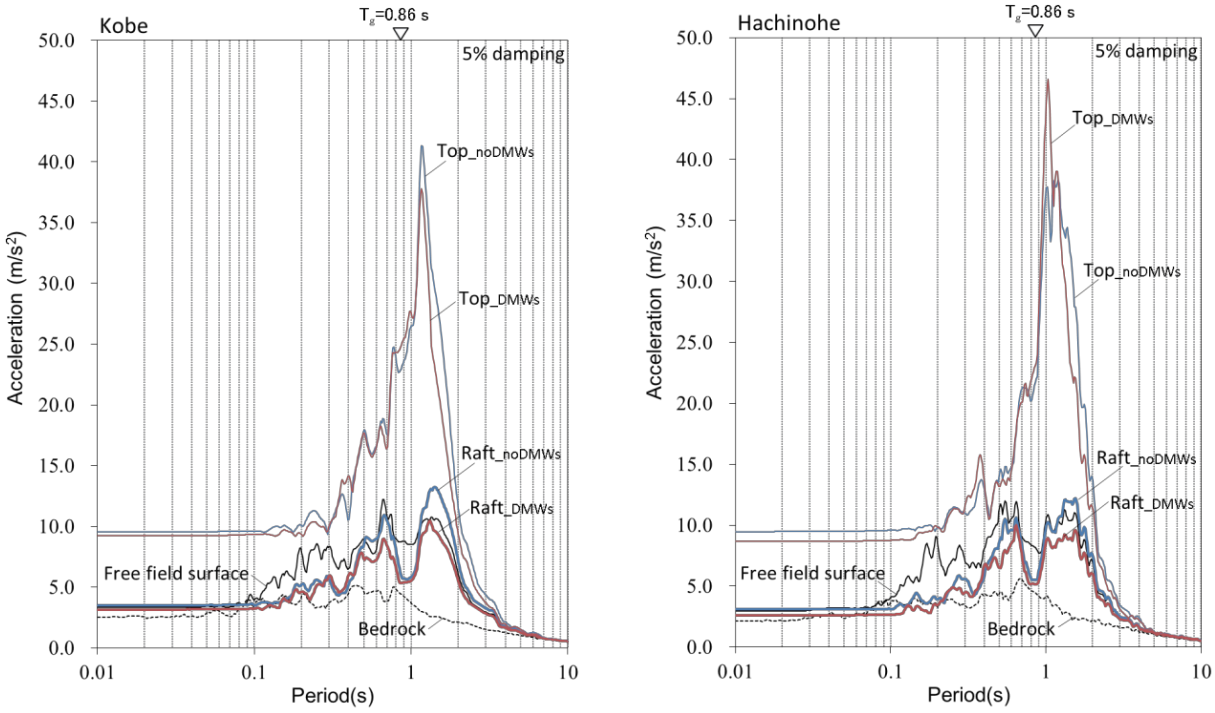

(a) LS model (T_b=0.87 s)

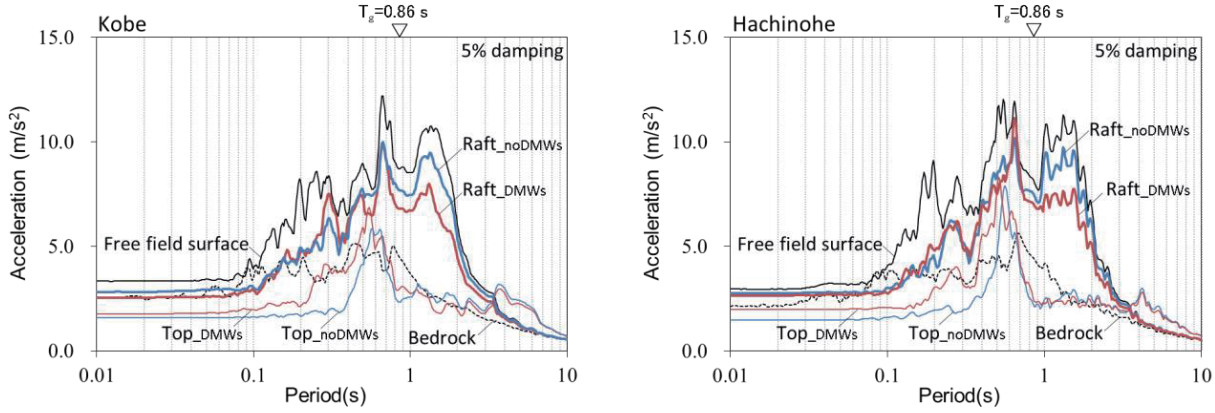

(b) BI model (T_b=4.6 s)

Fig. 9 Acceleration response spectra: top of structure at center, raft at point A and free-field ground surface

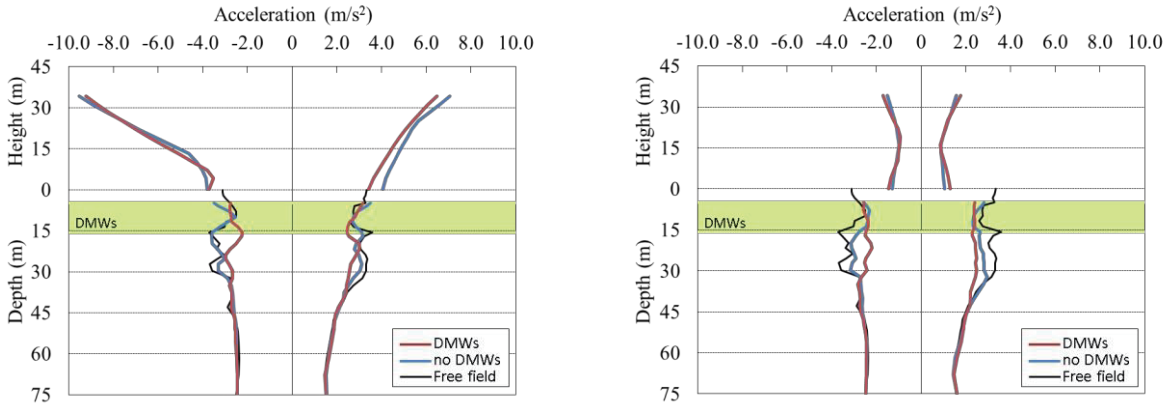

(a) LS model (b) BI model

Fig. 10 Peak acceleration profiles: superstructure at center, DMWs and ground under point A, and free field (Kobe phase)

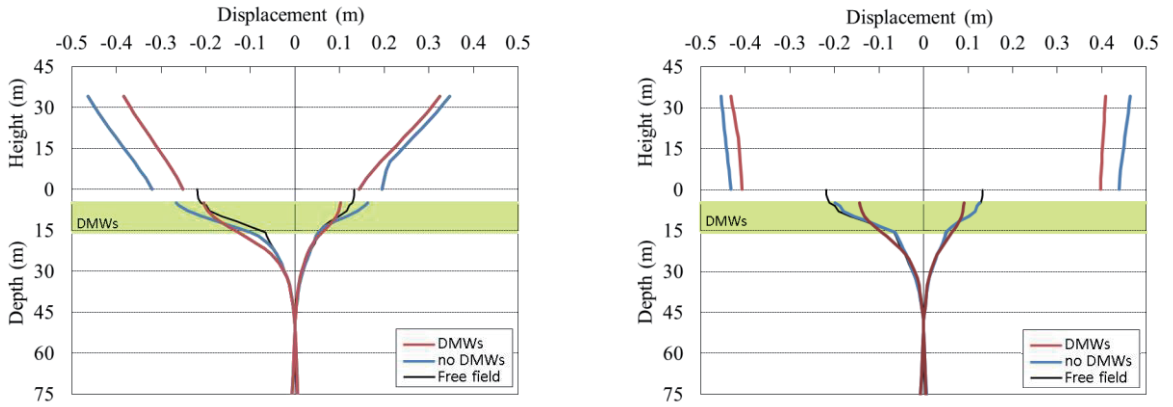

(a) LS model (b) BI model

Fig. 11 Peak lateral displacement profiles: superstructure at center, DMWs and ground under point A, and free field (Kobe phase)

Figure 12 shows the peak bending moment profiles of Pile 5B (1.2 m in diameter) and Piles 5A and 7B (1.0 m) under the Kobe phase. The maximum bending moments are generated at the pile head, excepting to Pile 5A in the case with DMWs and Pile 7B in BI model with DMWs. The maximum moments in Piles 5A and 7B are generated at depths of 9.9 m and 15.7 m, respectively. This ocurrs probably due to the interaction between the piles and the DMWs, considering that Piles 5A and 7B are located adjacent to the DMWs. In both LS and BI models, it appears that the peaks in the case with DMWs are significantly less than those without DMWs not only near the pile head but also to some depth deeper than the DMWs bottom.

Figure 13 shows the incremental axial forces along the piles under the Kobe phase (compression is positive). The solid line indicates the greater value out of the compressive and tensile ones. The incremental axial forces in LS model are significantly greater than those in BI model possibly due to the large overturning moment of the superstructure. The incremental forces at the pile head in Pile A located at the edge in the shaking direction are relatively large in both models. The incremental forces at the pile head in the case with DMWs are less than those without DMWs in LS model, while vice versa in BI model. In addition, the incremental forces at the pile head are close to the maximum values but not necessarily the maximums.

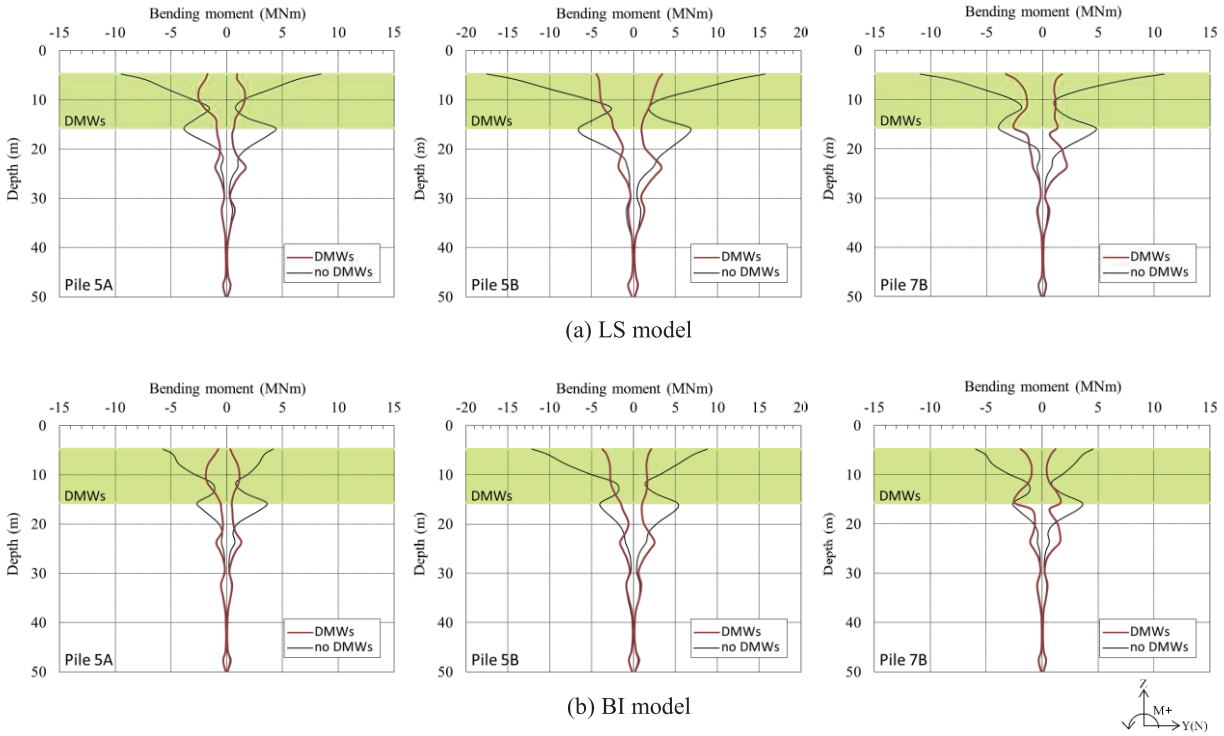

(a) LS model

(b) BI model

Fig. 12 Profiles of peak bending moment of piles (Kobe phase)

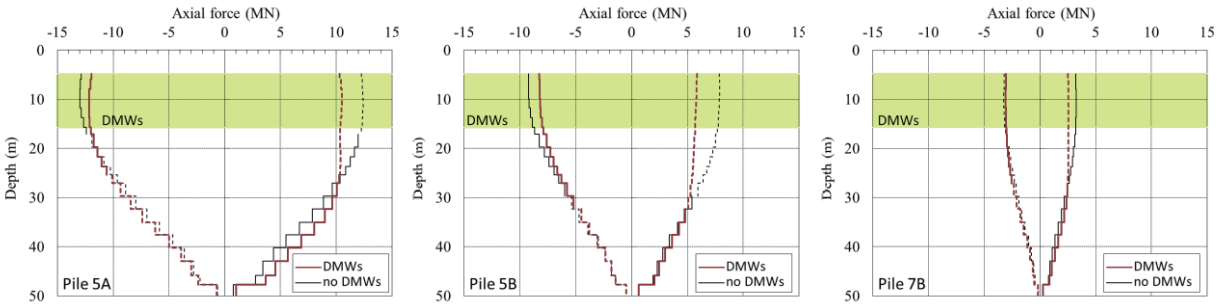

(a) LS model

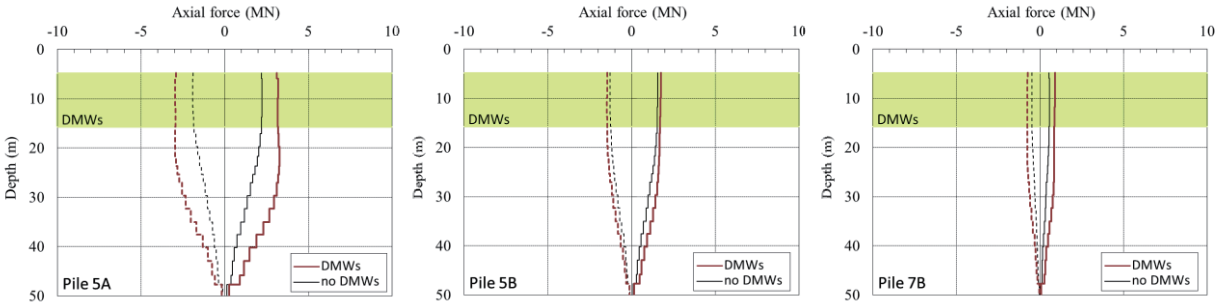

(b) BI model

Fig. 13 Profiles of peak axial force of piles (Kobe phase)

Figure 14 shows the time histories of the accelerations of the free-field ground and structure, the inertial forces of the superstructure and raft, the horizontal displacements of the ground and raft, the earth pressure resultant, the sum of shear forces at the pile head, the bending moment and incremental axial force of the piles under the Kobe phase during 30-40 s (including the peaks) in LS model, and Fig. 15 shows those in BI model. The earth pressure resultant means the sum of active and passive earth pressure and friction acting on the raft side. The bending moments are those at the pile head, exceping to the cases of Pile 5A with DMWs. For the Pile 5A with DMWs, the bending moments are those at 9.9 m depth where the maximum moment is generated. The incremental axial forces are those at the pile head. The inertial forces of the superstructure and the raft, the earth pressure resultant and the sum of shear forces at the pile head (additionally, the resistant forces of the soil and the DMWs shown in Figs. 18 and 19) were obtained in the same way which is mentioned in the previous numerical study. Note that these values are obtained assuming that damping forces are neglected.

The red dashed line indicates the time when the maximum acceleration of the ground at the surface occurs (t=35.01 s). The maximum ground acceleration does not occur simultaneously with the maximum accelerations of the top of the structure nor with the maximum superstructure inertial forces in both LS and BI models. The maximum superstructure inertial forces occur almost simultaneously with the maximum acceleration of the top of the structure in LS model. In both LS and BI models, the time histories of the raft inertial force are similar and the maximum raft displacements occur almost simultaneously with the maximum ground displacement. The sum of shear forces at the pile head in the case with DMWs is remarkably small compared with that without DMWs. The maximum bending moments of the piles occur almost simultaneously with the maximum ground acceleration (or ground displacement) regardless of the presence of the DMWs. The maximum incremental axial forces at the pile head in LS model occur in tension and almost simultaneously with the maximum superstructure inertial forces, while no simultaneity between the two in BI model.

5 DISCUSSIONS

5.1 Inertial forces and kinematic ground movements

Resulting from Figs. 14 and 15, the relations of the ground surface displacement with the inertial force under the Kobe phase during 30-40 s are shown in Fig. 16. Open circles indicate the maximums of the displacement and inertial force. The maximum superstructure inertial forces in BI model are remarkably small, 15-18% of those in LS model. In LS model (in which T_g>T_b

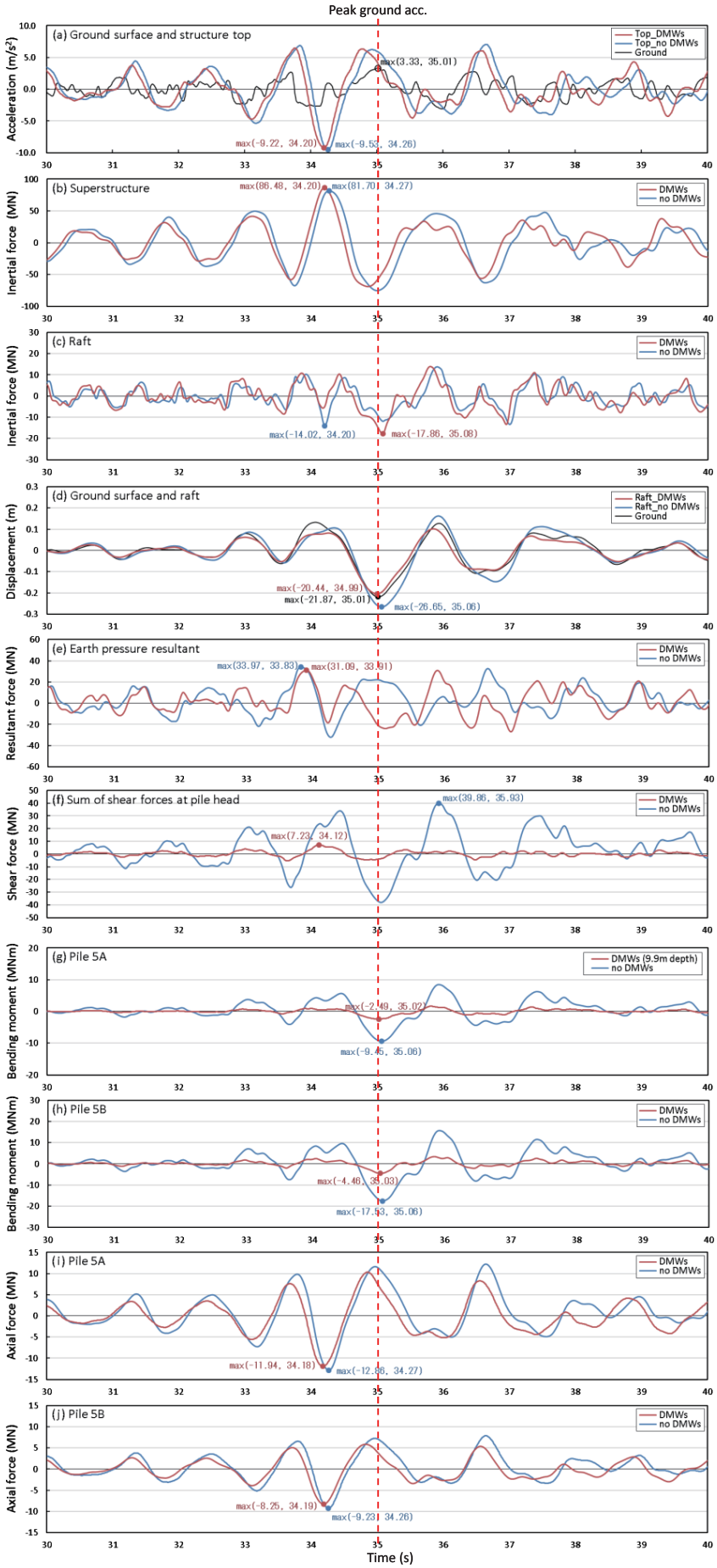

Fig. 14 Time histories of acceleration, inertial force, horizontal displacement, earth pressure resultant and pile sectional force in LS model (Kobe phase)

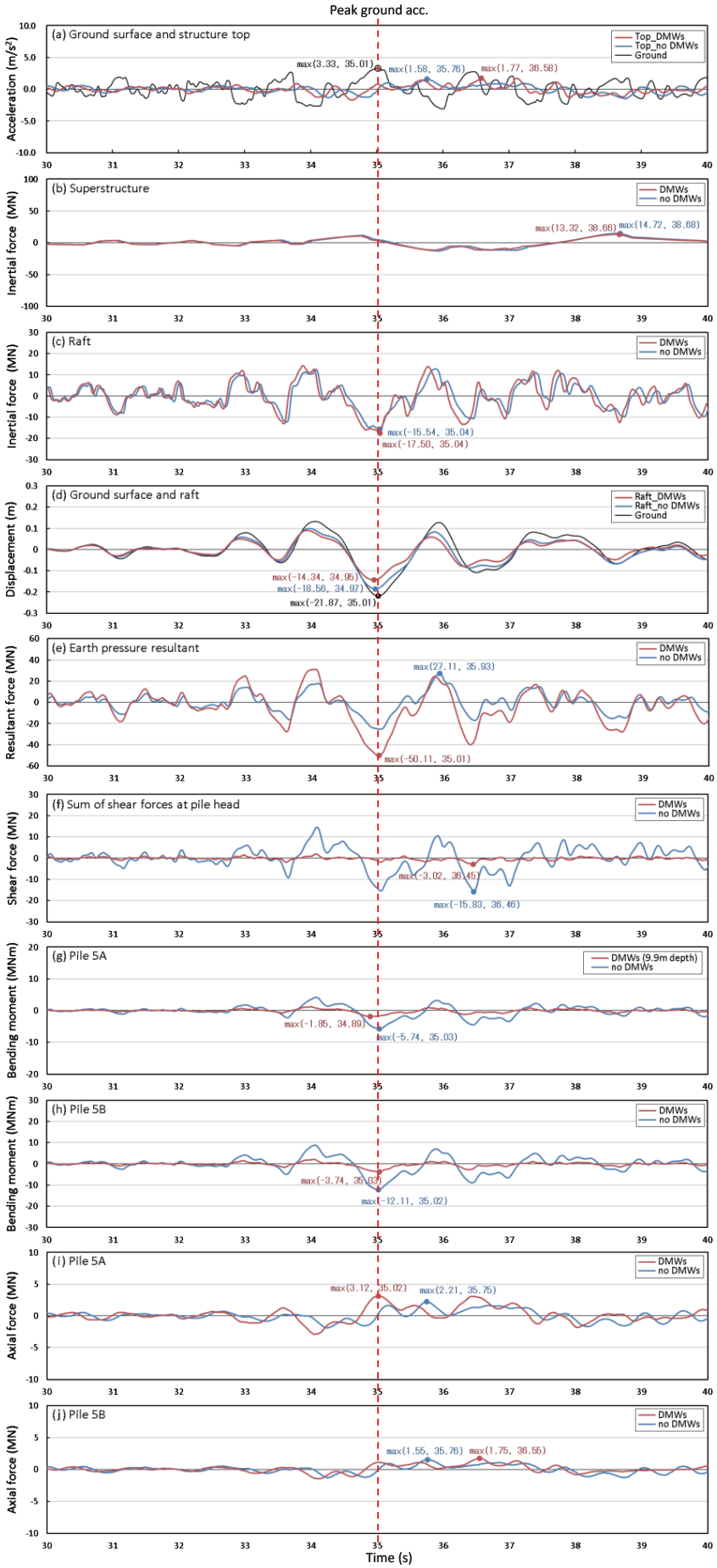

Fig. 15 Time histories of acceleration, inertial force, horizontal displacement, earth pressure resultant and pile sectional force in BI model (Kobe phase)

under Level 2 motions), the inertial forces of the superstructure and raft are generally in phase with the ground displacement regardless of the presence of the DMWs. Namely, the ground displacement acts in the same direction of the inertial forces, thereby increasing the lateral force transfered from the raft to the foundation elements. In BI model, the superstructure inertial force is nearly out of phase with the ground displacement. The raft inertial force is generally in phase with the ground displacement. Furthermore, the maximum raft inertial force occurs almost simultaneously with the maximum ground displacement regardless of the presence of the DMWs.

The earth pressure resultant is generated by both the inertial and kinematic effects. Tamura and Hida (2014) have reported, based on the dynamic centrifuge tests on a superstructure-footing model in sand, that the peaks of dynamic earth pressure resultant acting on the side of the embedded pile cap increased concurrently with the relative displacement between the pile cap and the soil. Note that the relative displacement incorprates both the inertial and kinematic effects. The relations of the relative displacement (δS-δR) with the earth pressure resultant are shown in Fig. 17. Here, δS is the ground surface displacement and δR is the raft displacement. The earth pressure resultants have relatively strong correlation with the relative displacements regardless of the presence of the DMWs, and the correlation between the two is quite similar in LS and BI models. These numerical results are consistent with the experimental results reported by Tamura and Hida (2014).

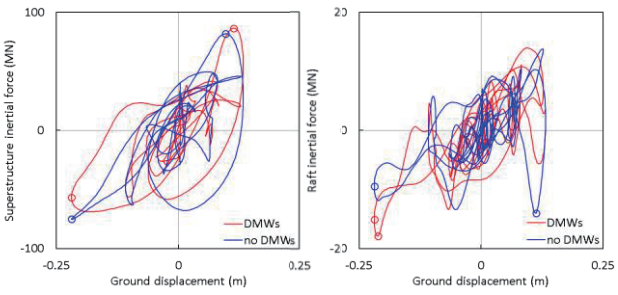

(a) LS model

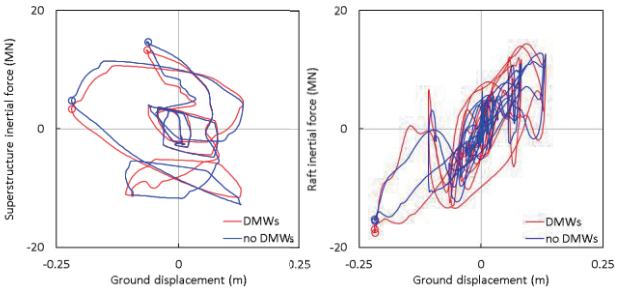

(b) BI model

Fig. 16 Ground surface displacement vs. inertial forces under Kobe phase (30-40 s)

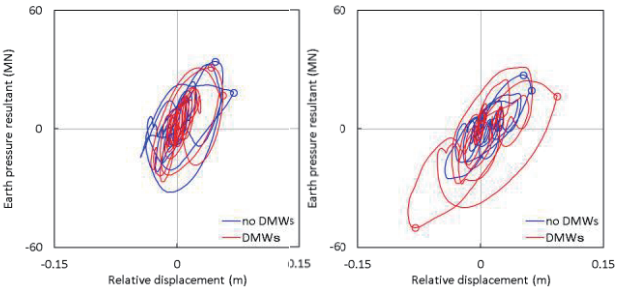

(a) LS model (b) BI model

Fig. 17 Relative displacement (ground disp.-raft disp.) vs. earth pressure resultant under Kobe phase (30-40 s)

5.2 Lateral load transfer mechanism

Figure 18 illustrates schematics of the deformation of the structure-foundation system in cross-section Y1-Y2 (shown in Fig. 2(b)) and the equilibrium of the lateral external and resistant forces at the raft bottom under the Kobe phase when the bending moment of Pile 5B is at its maximum (referred to as t_{M5Bmax}), where the external forces transferred from the raft (i.e., inertial forces of the superstructure and raft and the earth pressure resultant) with the resistant forces of the foundation elements (i.e., loads carried by the piles, the soil and the DMWs) are shown. Figure 19 shows the same illustrations as those given in Fig. 18 when the axial force at the pile head of Pile 5A is at its maximum (referred to as t_{N5Amax}).

At the time of t_{M5Bmax}, shear deformation of the ground and large curvature of the piles are seen to a depth of about 20 m from the raft bottom, while at the time of t_{N5Amax} such deformation is hardly seen. In LS model, the inertial forces of the superstructure at t_{N5Amax} (which are almost equal to their maximum) are considerably greater than those at t_{M5Bmax}. The earth pressure resultant in LS model without DMWs is in the opposite direction of the ground displacement both at t_{M5Bmax} and t_{N5Amax}, while the earth pressure resultant in BI model with DMWs is in the same direction of the ground displacement. This occurs because the raft displacement in the former is greater than the ground displacement both at t_{M5Bmax} and t_{N5Amax} as shown in Fig. 14(d), while the raft displacement in the latter is less than the ground displacement as shown in Fig. 15(d). The maximum earth pressure resultant is 50.1 MN (in BI model with DMWs shown in Fig. 15(e)) which is greater than but roughly consistent with the sum of the Rankine's active and passive earth pressure resultant and the ultimate side friction (0+23.2+19.2 =42.4 MN). The above sum was calculated with the shear strength of the soil near the surface (60 kPa) which was used in the FE analysis.

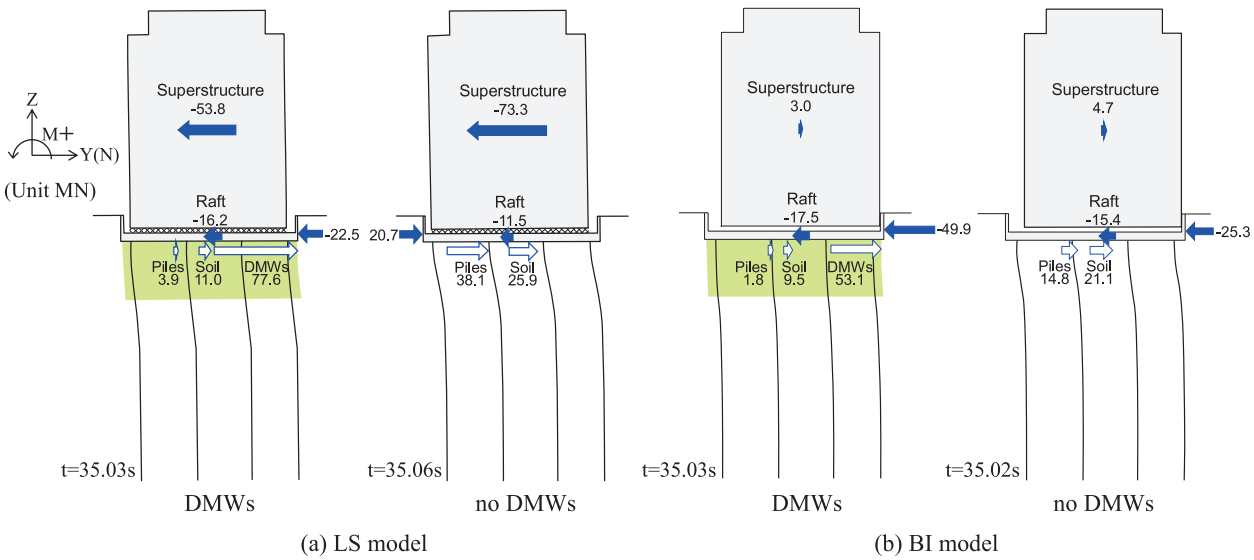

Fig. 18 Equilibrium of lateral forces at the raft bottom at t_{M5Bmax} under Kobe phase
(displacements enlarged by 10 times for foundation while 5 times for superstructure)

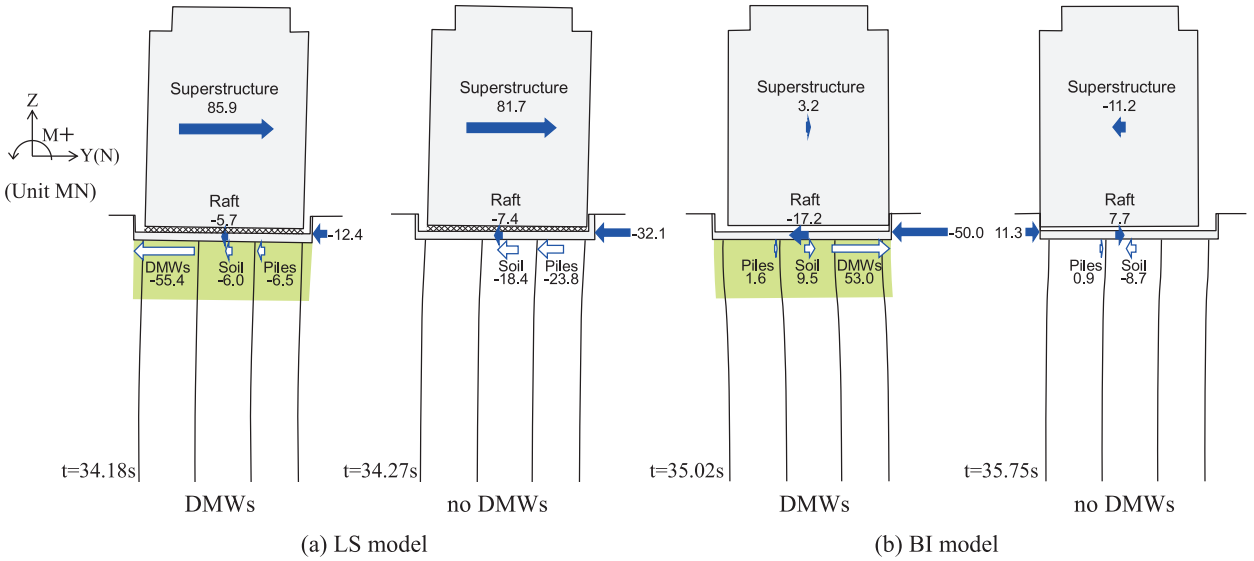

Fig. 19 Equilibrium of lateral forces at the raft bottom at t_{N5Amax} under Kobe phase
(displacements enlarged by 10 times for foundation while 5 times for superstructure)

Figures 18 and 19 indicate that the lateral loads carried by the piles in the case with DMWs are very small compared to those without DMWs. Moreover, as indicated in Fig. 12, the bending moments of piles in the case with DMWs are decreased significantly not only near the pile head but also to some depth deeper than the DMWs bottom. This arises because the amplification of the ground movement below the raft is restrained by the DMW grid in addition that the most part of the lateral force transferred from the raft (the sum of the inertial forces of the superstructure and raft and the earth pressure resultant) is carried by the DMWs, as pointed out by Yamashita et al. (2018).

Figure 20 shows the relations of the lateral force transferred from the raft with the sum of shear forces at the pile head. The maximum values of the lateral force from the raft and those of the sum of shear forces at the pile head are listed in Table 4. The lateral forces from the raft in BI model are significantly small, 68% and 57% of those in LS model with DMWs and without DMWs, respectively. In both models, the maximum lateral forces in the case with DMWs are considerably greater than those without DMWs. This may be attributed to the effect of the earth pressure resultant acting on the raft side as is seen in Figs. 18 and 19. The sum of the shear forces at the pile head in BI model are about 40% of those in LS model, though the maximum superstructure inertial forces in BI model are 15-18% of those in LS model. This implies that the kinematic effect on the sectional force of piles connected to the raft embedded in soft ground is relatively large. The sum of shear forces at the pile head in the

Table 4 Lateral force from the raft and sum of shear forces at the pile head

	LS model		BI model	
	DMWs	no DMWs	DMWs	no DMWs
Lateral force from raft (MN)	94.0	64.0	64.3	36.5
Sum of shear forces at pile head (MN)	7.2	39.9	3.0	15.8
Ratio of shear force to lateral force	0.08	0.62	0.05	0.43

case with DMWs are 5-8% of the lateral force from the raft, while in the case without DMWs the sum of shear forces are 43-62% of the lateral force. According to the dynamic model test results of piled raft combined with soil-cement walls supporting a slender building in soft clayey soil using a geotechnical centrifuge reported by Hamada et al. (2019), since most part of the inertial force of the structure was transferred to the soil-cement walls, the ratio of the sum of shear forces at the pile head to the inertial force was significantly small, only about 1% under a small earthquake and about 10% even under a strong earthquake. The numerical results in the case with DMWs are consistent with the dynamic model test results reported by Hamada et al. (2019).

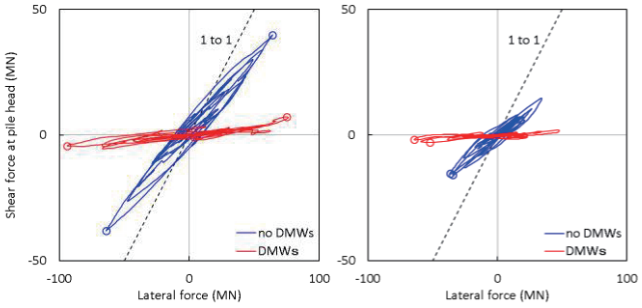

(a) LS model (b) BI model

Fig. 20 Lateral force from raft vs. sum of shear forces at pile head under Kobe phase (30-40 s)

It is noted that when the sum of the lateral forces is greater than the frictional resistance between the raft and the DMWs, it is possible that the load carried by the piles increases due to a slip of the raft. The possibility of the slip is roughly examined, based on the monitoring results of the 12-story building (Yamashita et al., 2012) and coefficients of friction between cement-stabilized soil and concrete obtained from the model tests reported by Tanikawa et al. (2015). The frictional resistance was estimated using the effective contact pressure (the contact pressure minus the pore-water pressure) between the raft and the DMWs of 265 kPa and the coefficient of friction of 0.8-1.0. The frictional resistance between the raft and the DMWs (area of 250 m^2) is calculated to be 53-66 MN. These values are comparable with or greater than the maximum load carried by the DMWs of 53.1 MN in BI model, however, less than that of 77.6 MN in LS model. Tanikawa et al. (2015) found that when the mechanical joint with dents and bumps was added between the cement-stabilized soil and concrete, an equivalent coefficient of friction became more than 1.2. When the mechanical joint is considered in the LS model, the frictional resistance is calculated to be more than 79 MN, greater than the maximum load (77.6 MN).

5.3 Inertial and kinematic effects on pile sectional force

Figure 21 shows the relations of the inertial force with the bending moment of Pile 5B at the pile head under the Kobe phase. In LS model, the bending moment is generally in phase with the superstructure inertial force while the correlation between the two in BI model is low. In both LS and BI models, the bending moment is generally in phase with the raft inertial force. In BI model, the maximum bending moment occurs simultaneously with the maximum raft inertial force regardless of the presence of the DMWs. Figure 22 shows the relations of the ground surface displacement with the bending moment of Pile 5B at the pile head. In both LS and BI models, the bending moment is in phase with the ground displacement and the maximum bending moment occurs simultaneously (or almost simultaneously) with the maximum ground displacement.

Figure 23 shows the relations of the inertial force with the incremental axial force of Pile 5A at the pile head. In LS model, the incremental axial force has strong correlation with the superstructure inertial force, and the maximum axial force occurs simultaneously with the maximum superstructure inertial force. On the other hand, in BI model the incremental axial force has no significant correlation with the superstructure inertial force. In both LS and BI models, the incremental axial force has no significant correlation with the raft inertial force. Figure 24 shows the relations of the ground-surface displacement with the incremental axial force of Pile 5A at the pile head. The incremental axial force tends to be tensile as the ground displacement increases excepting to BI model without DMWs.

Figure 25 shows the relations of the axial force with the bending moment under Kobe phase. The incremental axial force and bending moment are those at the pile head, exceping to Pile 5A in the case with DMWs in which the axial force and bending

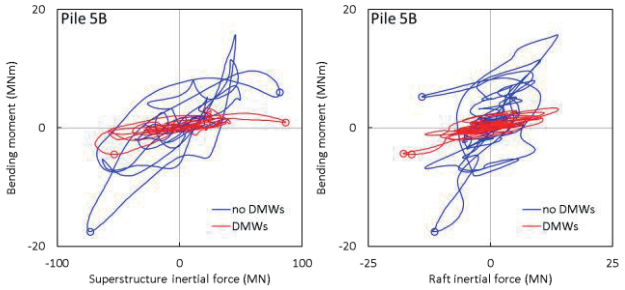

(a) LS model

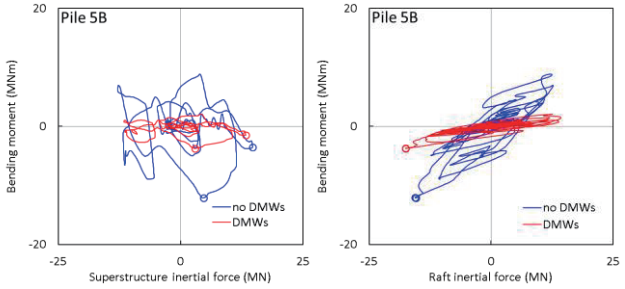

(b) BI model

Fig. 21 Inertial force vs. bending moment at pile head under Kobe phase (30-40 s)

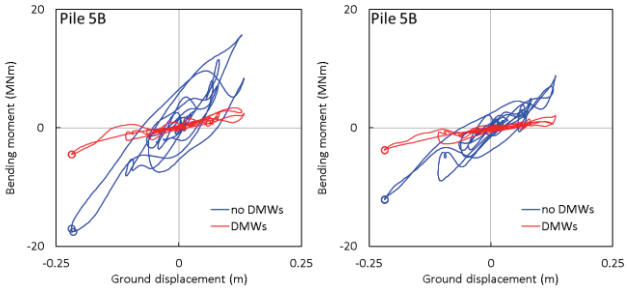

(a) LS model (b) BI model

Fig. 22 Ground surface displacement vs. bending moment at pile head under Kobe phase (30-40 s)

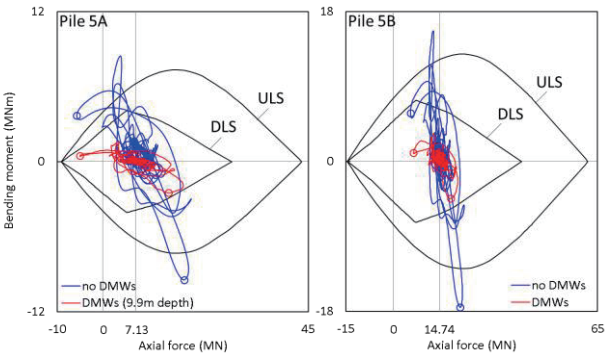

(a) LS model

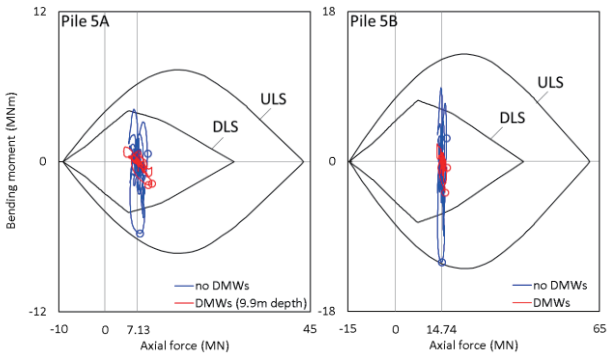

(b) BI model

Fig. 25 Axial force vs. moment relations under Kobe phase with design NM-interaction curves (30-40 s)

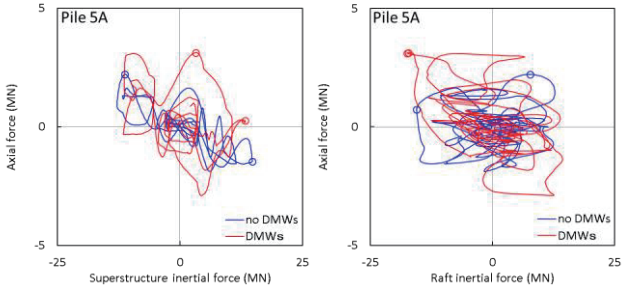

(a) LS model

(b) BI model

Fig. 23 Inertial force vs. incremental axial force at pile head under Kobe phase (30-40 s)

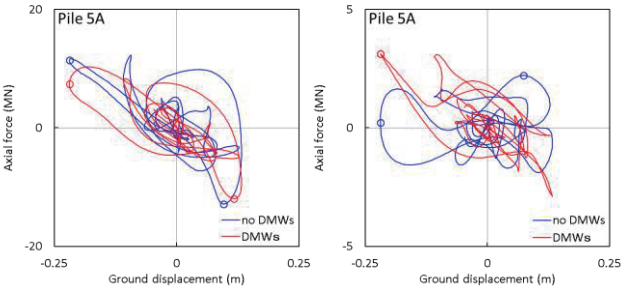

(a) LS model (b) BI model

Fig. 24 Ground surface displacement vs. incremental axial force at pile head under Kobe phase (30-40 s)

moment are those at 9.9 m depth as indicated in Fig. 25. The axial force is the sum of the initial axial force near the pile head and the dynamic incremental force. The initial axial forces were estimated based on the field monitoring of the 12-story building (Yamashita et al., 2015). In LS model without DMWs, the bending moments are so large that the sectional forces of both the piles exceed completely the ultimate limit state (ULS) of the SC pile. In LS model with DMWs, the sectional forces of both the piles are within the damage limit state (DLS). In Pile, 5A, the maximum increments of the axial force in tension exceed the initial axial force (7.13 MN) regardless of the presence of the DMWs, but the net tensile forces are much less than

the ultimate shaft resistance. In BI model without DMWs, the sectional forces of the piles are within but close to the ULS, while in BI model with DMWs the sectional forces are within the DLS.

In order to evaluate the kinematic effect on the sectional force of the piles independently, the numerical analyses of null mass model (shown in Table 3), in which the mass of the superstructure, raft and piles are not considered, were conducted. Figure 26 shows the relations of the axial force with the bending moment in Piles 5A and 5B from the null mass model analysis, which are superimposed on those of the axial force with the bending moment shown in Fig. 25. The maximum bending moments in the null mass model are 57-67% of those in LS model without DMWs, and 75-79% of those with DMWs. Hence, it was found that the bending moments of piles in the piled raft are more affected by the kinematic ground movement than the inertial force from the structure regardless of the presence of the DMWs, though the inertial forces from the superstructure in LS model are large as shown in Fig. 16. The incremental axial forces in the null mass model are quite small compared to those in LS model. Hence, the incremental axial forces in LS model are generated almost entirely by the inertial force from the structure. On the other hand, the maximum bending moments in the null mass model are 94-100% of those in BI model regardless of the presence of the DMWs, and the maximum values of the bending moment as well as the incremental axial force in the null mass model are approximately equal to those in BI model. Thus, the bending moment and the incremental axial force of piles are generated mostly by the kinematic effect.

5.4 Internal stress in DMWs

Figure 27 illustrates the extent of tensile failure in the DMW grid under Kobe phase. The elements are shaded according to the number of Gauss points at which tensile failure occurs. The tensile failure in LS model is seen in the extensive portion at the bottom of the longitudinal walls (parallel to the shaking direction), while the tensile failure in BI model is in the limited portion at the bottom. This occurs probably because the lateral load carried by the DMWs in the former is considerably larger than that in the latter as shown in Fig. 18. It should be noted that the strain softening characteristics of the stabilized soil, which is not considered in the present analysis, occurs after the tensile stress reaches the tensile strength as pointed out by Namikawa et al. (2007). Further studies on the strain softening characteristics are necessary to understand the seismic performance of the DMWs under strong earthquakes more accurately (Shigeno et al., 2019).

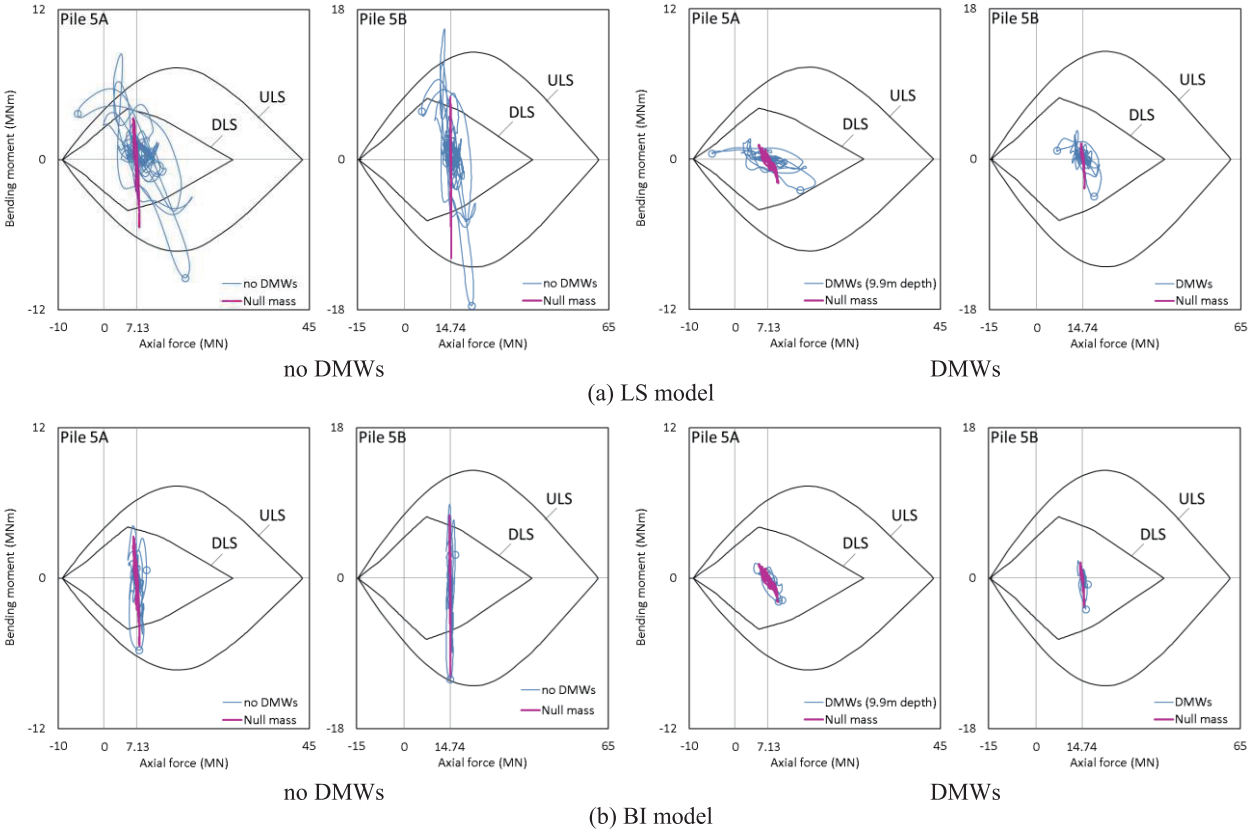

Fig. 26 Axial force vs. moment relations from null mass model with those from LS and BI models under Kobe phase (30-40 s)

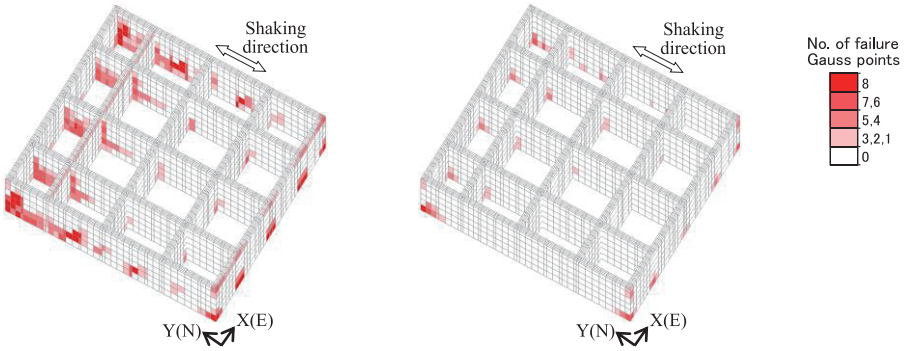

(a) LS model (b) BI model

Fig. 27 Extent of tensile failure in DMWs under Kobe phase

6 CONCLUSIONS

Based on the results from the seismic response analysis of the soil-piled raft-superstructure system in which natural periods of the superstructure are different, the following conclusions can be drawn:

(1) The maximum superstructure inertial forces in BI model in which the natural period of the superstructure (T_b) is fully larger than that of the ground (T_g) are markedly small, 15-18% of those in LS model in which T_b is near T_g. In LS model, the inertial forces of the superstructure and the raft are generally in phase with the ground displacement regardless of the presence of the DMWs, thereby increasing the lateral force transferred from the raft to the foundation elements. In BI model, the superstructure inertial force is nearly out of phase with the ground displacement. As a result, the lateral forces from the raft in BI model are significantly small, 68% and 57% of those in LS model with DMWs and without DMWs, respectively. In the case without DMWs, the sectional forces of the piles in LS model exceed completely the ULS, and those in BI model are within but close to the ULS.

(2) In both models, the sum of shear forces at the pile head in the case with DMWs are 5-8% of the lateral force transferred from the raft, while in the case without DMWs the sum of shear forces are 43-62% of the lateral force. The bending moments of piles in the case with DMWs are decreased significantly compared to those in the case without DMWs not only near the pile head but also to some depth deeper than the DMWs bottom. This arises because the amplification of the ground movement below the raft is restrained by the DMW grid in addition that the most part of the lateral force transferred from the raft is carried by the DMWs, as pointed out by Yamashita et al. (2018).

(3) A possibility of a slip between the raft and the DMWs under L2 motions was examined using the monitoring results of the building and the published values of coefficients of friction between cement-stabilized soil and concrete. It was found that the frictional resistance is less than the lateral force transferred from the raft in LS model while the frictional resistance is comparable or greater than the lateral force in BI model. In the former case, when the mechanical joint is added to the interface between the raft and the DMWs, the frictional resistance could be greater than the lateral force.

(4) In order to evaluate the kinematic effect on the sectional force of the piles independently, the bending moments and the incremental axial forces were compared with those obtained from the analysis of the null mass model in which the mass of the structure and piles are not considered. It was found that although the inertial forces from the superstructure in LS model are large, the bending moments of piles in the piled raft are more affected by the kinematic ground movement than the inertial force from the structure regardless of the presence of the DMWs. The incremental axial forces in LS model are generated almost entirely by the inertial effect. In BI model, both the bending moments and incremental axial forces of the piles are generated mostly by the kinematic effect regardless of the presence of the DMWs.

REFERENCES

Building Standard Law of Japan, 2000. Notification No. 1461 of the Ministry of Construction (in Japanese).

Hamada, J., Shigeno, Y., Onimaru, S., Tanikawa, T., Nakamura, N. and Yamashita, K., 2014. Numerical analysis on seismic response of piled raft foundation with ground improvement based on seismic observation records, Proc. of the 14th Int.

Assoc. Computer Methods and Recent Advances in Geomechanics, Kyoto, 719-724.

Hamada, J., Okumura, T. and Honda, T., 2019. Centrifuge model tests on seismic behavior of piled raft foundation with soil-cement wall in soft clayey ground, Proc. of the 7th Int. Conf. on Earthquake Geotechnical Engineering, Roma, 2787-2794.

Motojima, M., Hibino S. and Hayashi, M., 1978. Development of computer program for stability analysis of excavation, Central Research Institute of Electric Power Industry Report No 377012 (in Japanese).

Namikawa, T., Koseki, J. and Suzuki, Y., 2007. Finite element analysis of lattice-shaped ground improvement by cement-mixing for liquefaction mitigation, Soils & Foundations, Vol. 47 (3), 559-576.

Poulos, H. G., 2016. Lessons learned from designing high-rise building foundations, Geotechnical Engineering J. the SEAGS & AGSSEA, Vol. 47 (4), 35-49.

Poulos, H. G., 2017. Tall Building Foundation Design, CRS Press.

Shigeno, Y., Hamada, J. and Nakamura, N., 2014. Hybrid parallelization of earthquake response analysis using K computer, Proc. of the 14th Int. Assoc. Computer Methods and Recent Advances in Geomechanics, Kyoto, 587-592.

Shigeno, Y., Yamashita, K. and Hamada, J., 2019. Numerical study on seismic behavior of a piled raft foundation with grid-form DMWs considering post-peak softening of stabilized soil, Proc. of the 7th International Conference on Earthquake Geotechnical Engineering, Roma, 4986-4994.

Shiomi, T., Shigeno, Y. and Zienkiewicz, O. C., 1993. Numerical prediction for model No. 1. Verification of Numerical Procedures for the Analysis of Soil Liquefaction Problems (eds. by Arulanandan & Scott), Balkema, 213-219.

Tamura, S. and Hida, T., 2014. Pile stress estimation based on seismic deformation method with embedment effects on pile caps, J. Geotechnical and Geoenvironmental Engineering, ASCE, Vol. 140, No.9, 04014049.

Tanikawa, T., Hamada, J. and Honda, T., 2015. Mechanical joints transmitting lateral force to grid-form soil improvement, the 15th Asian Regional Conference on Soil Mechanics and Geotechnical Engineering, Fukuoka, 1259-1262.

Tsujino, S., Yoshida, N. and Yasuda, S., 1994. A simplified practical stress-strain model in multi-dimensional analysis, Proc. of International Symposium on Pre-failure Deformation Characteristics of Geomaterials, Sapporo, 463-468.

Yamashita, K., Yamada, T. and Hamada, J., 2011. Investigation of settlement and load sharing on piled rafts by monitoring full-scale structures, Soils & Foundations, Vol. 51 (3), 513-532.

Yamashita, K., Hamada, J., Onimaru, S. and Higashino, M., 2012. Seismic behavior of piled raft with ground improvement supporting a base-isolated building on soft ground in Tokyo, Soils & Foundations, Vol. 52 (5), 1000-1015.

Yamashita, K., Tanikawa, T., Shigeno, Y. and Hamada, J., 2015. Vertical load sharing of piled raft with grid-form deep mixing walls, Proc. of Conference on Deep Mixing 2015, San Francisco, 437-446.

Yamashita, K., Shigeno, Y., Hamada, J. and Chang, D. W., 2018. Seismic response analysis of piled raft with grid-form deep mixing walls under strong earthquakes with performance-based design concerns, Soils & Foundations, Vol. 58 (1), 65-84.